



**HAL**  
open science

# Enhancement of the piezoelectric response of ZnO nanowires grown via PLI-MOCVD using post-deposition treatments through adjusted screening and surface effects

L. Legardinier, G. Ardila, I. Gélard, C. Jiménez, M. Weber, F. Donatini, V. Consonni

## ► To cite this version:

L. Legardinier, G. Ardila, I. Gélard, C. Jiménez, M. Weber, et al.. Enhancement of the piezoelectric response of ZnO nanowires grown via PLI-MOCVD using post-deposition treatments through adjusted screening and surface effects. *Nanoscale*, 2025, 17 (17), pp.10835-10849. 10.1039/D5NR00591D . hal-05364984

**HAL Id: hal-05364984**

**<https://hal.science/hal-05364984v1>**

Submitted on 14 Nov 2025

**HAL** is a multi-disciplinary open access archive for the deposit and dissemination of scientific research documents, whether they are published or not. The documents may come from teaching and research institutions in France or abroad, or from public or private research centers.

L'archive ouverte pluridisciplinaire **HAL**, est destinée au dépôt et à la diffusion de documents scientifiques de niveau recherche, publiés ou non, émanant des établissements d'enseignement et de recherche français ou étrangers, des laboratoires publics ou privés.



Distributed under a Creative Commons Attribution 4.0 International License

# Enhancement of the piezoelectric response of ZnO nanowires grown by PLI-MOCVD using post-deposition treatments through adjusted screening and surface effects

L. Legardinier<sup>1,2</sup>, G. Ardila<sup>2\*</sup>, I. Gélard<sup>1</sup>, C. Jimenez<sup>1</sup>, M. Weber<sup>1</sup>, F. Donatini<sup>3</sup>, and V. Consonni<sup>1\*</sup>

<sup>1</sup>Université Grenoble Alpes, CNRS, Grenoble INP, LMGP, F-38000 Grenoble, France

<sup>2</sup>Université Grenoble Alpes, Univ. Savoie Mont Blanc, CNRS, Grenoble INP, CROMA, F-38000 Grenoble, France

<sup>3</sup>Université Grenoble Alpes, CNRS, Grenoble INP, Institut Néel, F-38000 Grenoble, France

## Abstract

As a biocompatible and non-critical material, ZnO, specifically in its nanowire morphology, holds great promise to be integrated into highly efficient mechanical energy transducers. However, the control of the density of free charge carriers driving the screening effect of the piezoelectric potential under mechanical solicitations is critical for enhancing their piezoelectric properties. To that extent, the effects of several post-deposition treatments, including O<sub>2</sub> plasma, UV ozone, and thermal annealing under O<sub>2</sub> atmosphere, on the properties of ZnO nanowires grown by pulsed-liquid injection metal-organic chemical vapor deposition are thoroughly investigated and compared. The thermal annealing at high temperature shows its predominance over the other post-deposition treatment for the decrease in the density of free electrons, roughly estimated from 1.8 – 3.3 x 10<sup>18</sup> to about 10<sup>17</sup> cm<sup>-3</sup>, the removal of carbon contamination inside the structure, and the crystallinity improvement. By proceeding with the thermal annealing and increasing its temperature from 700 to 900 °C, time-resolved cathodoluminescence measurements further reveals the decrease in the density of surface traps from 7.7 to 3.0 x 10<sup>12</sup> cm<sup>-2</sup> due to an increase in the amount of oxygen vacancies at the surfaces of ZnO nanowires. The effective piezoelectric coefficient  $d_{33}^{eff}$  as measured by piezo-response force microscopy eventually shows a significant enhancement of 47 %, from 4.5 to 6.6 pm/V, as the annealing temperature and duration are increased. These findings reveal the trade-off to optimize when using the post-deposition treatments, as supported by finite element method simulations, which show that the reduction of both the densities of free electrons and of surface traps act in an opposite manner on the piezoelectric response of ZnO nanowires.

**Keywords:** zinc oxide, piezoelectricity, nanowires, metal-organic chemical vapor deposition, plasma, UV ozone, thermal annealing

**\*Corresponding Authors:** [gustavo.ardila@grenoble-inp.fr](mailto:gustavo.ardila@grenoble-inp.fr) and [vincent.consonni@grenoble-inp.fr](mailto:vincent.consonni@grenoble-inp.fr)

## 1. Introduction

Zinc oxide (ZnO), known for its abundance as a compound semiconductor, has found widespread potential applications in various domains, including UV light-emitting diodes and lasers [1], [2], UV photodetectors [3], [4], as well as piezoelectric and piezotronic components [5], [6]. The attention to ZnO for piezoelectric applications is justified by its eco-friendly and sustainable nature, contrary to the commonly used lead zirconate titanate (PZT) material [7], and by its relatively high piezoelectric coefficients as compared to alternative compound semiconductors [8]. ZnO has thus been developed in various piezoelectric devices, especially in the form of nanowires (NWs), showcasing a promising potential in piezoelectric nanogenerators [9], [10], [11], [12]. However, a significant challenge in employing ZnO for piezoelectric applications relies on its high residual n-type doping. The incorporation of numerous residual impurities occurs during the growth of ZnO, regardless of the deposition techniques employed [13]. These impurities act as shallow donors with a low formation energy, introducing a substantial number of free electrons into the ZnO structure. The migration of these free electrons results in the screening of the piezoelectric potential generated under mechanical solicitations, leading to a significant reduction in the amplitude of the piezoelectric response [14]. Nevertheless, oxygen is known to efficiently adsorb on the surfaces of ZnO, creating a depletion region in their vicinity. This effect has an important impact on the piezoelectric properties, by compensating for the screening effect coming from the high density of free electrons [15]. The NW morphology further allows to increase the available surface area, making it an asset in piezoelectric applications. Therefore, mitigating the density of free electrons while optimizing the presence of surface traps become imperative to enhance the piezoelectric efficiency of ZnO NWs in practical piezoelectric applications [16]. Various growth methods can be employed to grow ZnO NWs, ranging from wet chemical processes like chemical bath deposition (CBD), to metal-organic chemical vapor deposition (MOCVD) [17], [18], [19], [20]. This latter technique is particularly interesting for its ability to facilitate rapid NW growth across a substantial surface area, while preserving exceptional optical and structural properties. However, the predominant focus of research has been on using an MOCVD reactor equipped with a bubbler system mainly for optoelectronic applications [21], [22].

The pulsed-liquid injection MOCVD (PLI-MOCVD) has the advantage of working with a liquid zinc precursor kept at room temperature and allows the use of a lower growth temperature, while precisely controlling the flow rates of chemical precursors injected in the chamber [20], [23], [24]. Until now, the development of ZnO NWs grown by PLI-MOCVD specifically for piezoelectric applications has nevertheless been poorly explored. The effects of the radius of ZnO NWs over a

range of 18 - 103 nm have recently been shown on their structural, optical, electrical and piezoelectric properties, from which a high density of free electrons and of surface traps in the ranges of  $1.8\text{--}3.3 \times 10^{18} \text{ cm}^{-3}$  and  $5 \times 10^{12}\text{--}1.0 \times 10^{13} \text{ cm}^{-2}$  were respectively determined [25]. Generally, the post-deposition treatments are highly efficient to optimize the optical and electrical properties of ZnO NWs, but their effect on the densities of free electrons and of surface traps along with the impact on the correlated magnitude of the piezoelectric response has never been investigated so far. In this work, O<sub>2</sub> plasma, UV ozone, and thermal annealing under O<sub>2</sub> atmosphere are separately achieved using different durations and temperatures. These three post-deposition treatments have shown to remove the carbon contamination in ZnO materials [26], [27], [28], therefore improving their crystallinity and purity. A previous study further reported a change in the surface band bending and Fermi level after O<sub>2</sub> plasma treatment [27], impacting the density of surface traps. The regulation of the electrical properties after UV ozone was also shown in Ref [29]. An increase in the piezoelectric response of ZnO thin films after thermal annealing was demonstrated in Ref [28], but no correlation with the densities of free electrons and of surface traps was reported. The effect of these post-deposition treatments on the characteristics of ZnO NWs grown by PLI-MOCVD, including their structural, optical, electrical, and piezoelectric properties thus needs a further thorough investigation.

In this work, a broad range of post-deposition treatments including O<sub>2</sub> plasma, UV ozone, and thermal annealing at different temperatures from 700 to 900 °C under O<sub>2</sub> atmosphere is performed on ZnO NWs grown by PLI-MOCVD. The electrical properties of ZnO NWs are assessed by tunneling atomic force microscopy (TUNA), estimating the variation of the electrical resistivity and hence of the density of free charge carriers after post-deposition treatments. The structural and optical properties of ZnO NWs are studied by field-emission scanning electron microscopy (FESEM), low-temperature cathodoluminescence (CL) spectroscopy in both continuous and time-resolved modes, Raman spectroscopy and X-ray photoelectron spectroscopy (XPS), determining the evolution of the nature and amount of defects along with the density of surface traps after post-deposition treatments. The impact on the piezoelectric properties of ZnO NWs is eventually assessed by piezoresponse force microscopy (PFM) and analyzed through the support of finite element method (FEM) simulation, highlighting the significant roles of the density of free charge carriers and of the density of surface traps along with the necessary trade-off to be established for piezoelectric devices.

## 2. Experimental procedures

**ZnO nanowire growth.** ZnO NWs were synthesized using a PLI-MOCVD technique within an ANNEALSYS MC-200 reactor, on heavily p-type doped Si (100) substrates. In association with O<sub>2</sub> gas, a

precursor liquid solution of diethylzinc (DEZn,  $\text{Zn}(\text{C}_2\text{H}_5)_2$ ) was employed. Specifically, a 100 mL DEZn solution at a concentration of 1 M was diluted in cyclohexane ( $\text{C}_6\text{H}_{12}$ ), resulting in a concentration of 0.43 M. This diluted DEZn solution was introduced into the reactor chamber, with an Ar gas carrier, at flow rates of 0.5 g/min and 500 sccm, respectively. The flow rate of  $\text{O}_2$  gas was maintained at 300 sccm, leading to an O/Zn ratio of 48. Throughout the growth process, the chamber's pressure was held at 3 mbar. The substrate was heated to 700 °C, rotating at 30 rpm, and the growth was executed for 30 minutes.

**Post-growth treatments.** The  $\text{O}_2$  plasma treatments were performed using an EVACTRON decontaminator, generating a radio frequency (RF) plasma with a power of 12 W and a pressure of 0.4 torr, for 10 and 30 minutes. The UV ozone treatments were achieved using a NOVASCAN TECHNOLOGIES PSDP-UV8 digital UV ozone cleaner equipped with a PSD-TempOption thermal stage. The samples were placed for 20 minutes and 1h in the center of the aluminum foil of the UV ozone cleaner, where the temperature was measured around 70 °C owing to the heating from the Hg lamp. No additional exposure temperature was used for the UV ozone treatments. The thermal annealing was done in a CARBOLITE STF 16/180 tubular furnace under an  $\text{O}_2$  atmosphere using a flow rate of 2 L/min, for 1 and 2h, at a temperature in the range of 700-900 °C and with a heating gradient of 15 °C/min. The samples were placed in the center of the furnace using a recrystallized alumina boat, and removed when the temperature cooled down to approximately 250 °C.

**Structural property characterization.** Cross-sectional and top-view images of the ZnO NWs were conducted utilizing a Gemini 300 Field Emission ZEISS SEM. Raman spectroscopy measurements were carried out at room temperature, employing an excitation Ar<sup>+</sup> laser at 514.5 nm, and a 100X lens. A JOBIN YVON / HORIBA Labram spectrometer equipped with a liquid nitrogen-cooled CCD detector facilitated the Raman spectroscopy analysis. XPS were collected employing a THERMOSCIENTIFIC K-Alpha spectrometer featuring a monochromatized Al K $\alpha$  radiation source with an energy of 1486.6 eV, within an ultrahigh vacuum environment, specifically at a pressure of  $10^{-8}$  mbar and at room temperature. To ensure precision, the X-Ray beam area, or spot size, was finely tuned to a diameter of 400  $\mu\text{m}$ . The acquisition of spectra transpired in the constant analyzer energy mode, utilizing a pass energy of 30 eV and a step size of 0.1 eV for core levels. For the comprehensive survey spectrum, a pass energy of 100 eV was deployed with a step size of 0.5 eV. The spectra featured in the figures were derived from averaging, incorporating 3 scans for the survey and 10 scans for the core levels. To counteract charge effects on the surface, a flood gun was employed.

**Electrical property measurements.** TUNA measurements were conducted using a BRUKER Dimension Icon atomic force microscope (AFM). Platinum-coated silicon tips (PtSi-NCH from BRUKER)

were employed, featuring a spring constant ranging from 30 to 50  $\text{Nm}^{-1}$  and a resonance frequency between 204 and 497 kHz. The highly p-type doped Si (100) substrates on which the NWs were grown served as the bottom electrode. A bias voltage spanning from -5 V to 5 V was applied between the conductive tip and the substrate, and the current, detected while passing through the sample, exhibited a sensitivity of 100 nA/V. Mapping images were generated utilizing the DataCube TUNA mode. In this mode, the tip was retracted between each pixel after a 300 ms contact time with a constant deflection trigger of 40 nm to apply the bias voltage.

**Optical property measurements.** CL measurements were carried out using an FEI Inspect F50 FESEM instrument, with the electron beam at a voltage of 5 kV and a current of 22 pA. A magnification of 240 000X was used for the scanned surface ( $1.25 \times 1.25 \mu\text{m}^2$ ). The system was cooled at 5 K with liquid helium. The emitted signal was captured via a parabolic mirror, further analyzed using a Horiba iHR550 monochromator, and finally recorded by a Andor Technology Newton DU940 BU2 CCD detector. Time-resolved CL was done at room temperature using an electron beam with a 4 kV acceleration voltage and a 228 pA current, as well as a Hanbury Brown and Twiss interferometer equipped with two fast photomultiplier tubes (PMA Hybrid 06 from PicoQuant) exhibiting a time resolution smaller than 50 ps. The scanned area was of  $2.5 \times 2.5 \mu\text{m}^2$ .

**Piezoelectric property measurements.** PFM measurements were conducted using a BRUKER Dimension Icon AFM. For these measurements, the same tips as for TUNA measurements were used. The NWs were grown on highly p-type doped Si (100) substrates, which served as the bottom electrical contact. Dealing with rough surfaces, such as vertically aligned NWs, presented particular challenges, including the potential for scratching and bending of the NWs. Such challenges could lead to issues like contact failure between the tip and the sample. To address these challenges, we employed the DataCube PFM mode. In this mode, the tip was retracted between each pixel of the image. When the tip made contact with the sample, it remained in contact for 80 ms, while an AC voltage of 5 V was applied between the tip of the NW and the substrate. This allowed to capture the resulting piezoelectric deformation of the sample. The results presented for each pixel represent the mean value of the collected signals during this time period. PFM amplitude and phase measurements refer to the tip's oscillation amplitude at the frequency of the PFM modulation and the phase shift between the tip's mechanical oscillations and the PFM modulation voltage, respectively. The PFM modulation frequency was set within the range of 10-15 kHz, ensuring that the piezoelectric response amplitude and phase remained independent of frequency. This was done to prevent any undesired amplification of the piezoelectric response amplitude (parasitic effects) [20], [30], [31]. Additionally, the substantial stiffness of the tip played a role in preventing cantilever buckling and significantly reducing electrostatic interference with the piezoelectric response [32]. The

measurement was performed twice for each sample, on different zones. The amplitude of the piezoelectric response was calculated by filtering the data, such that only the values within a small square centered at the top surface of the ZnO NW, with a 20 nm<sup>2</sup> area, were retained to calculate its mean value, as in Ref. [25]. The standard deviation of these measurements was used to generate the error bars. This procedure was applied to three different NWs for each sample.

### 3. Results

#### 3.1. Effect of the post-deposition treatments on the morphology of ZnO nanowires

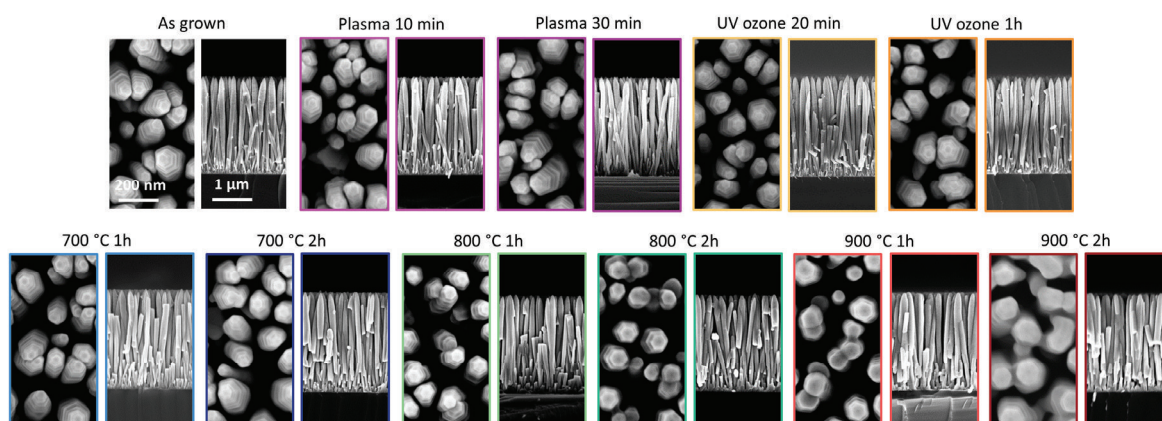


*Figure 1. Top-view and side-view FESEM images of ZnO NWs grown by PLI-MOCVD at 700 °C for 30 minutes and treated with O<sub>2</sub> plasma for 10 and 30 min, UV ozone for 20 min and 1h, and thermal annealing at 700 °C, 800 °C and 900 °C for 1 and 2h under O<sub>2</sub> atmosphere.*

ZnO NWs were grown by PLI-MOCVD at 700 °C for 30 min and exhibit a mean diameter and length of about 140 nm and 2.5 μm, respectively. Their pencil-shaped morphology with a faceted hexagonal section is typical from their growth along the polar *c*-axis by PLI-MOCVD.[20] After growth, several post-deposition treatments were achieved, such as O<sub>2</sub> plasma, UV ozone, and thermal annealing under O<sub>2</sub> atmosphere. The O<sub>2</sub> plasma treatment was done for both 10 and 30 min, while the UV ozone treatment was achieved for 20 min and 1h. Three annealing temperatures were chosen, including 700 °C, 800 °C and 900 °C for 1h and 2h by considering that the MOCVD process was performed at 700 °C. The annealing temperature of 700 °C was similar to the MOCVD process temperature, but the annealing time was much longer than the growth time of only 30 min. Top-view and side-view FESEM images of as-grown, treated, and thermally annealed ZnO NWs are shown in *Figure 1*. A higher magnification of each top-view and side-view FESEM image is presented in Figure S1-S6 of Supporting Materials. The dimensions of treated and thermally annealed ZnO NWs are similar to the dimensions of as-grown ZnO NWs, regardless of the post-deposition treatment conditions. The O<sub>2</sub> plasma and UV ozone treatments further have no impact on the morphology of ZnO NWs keeping their pencil shape with a faceted hexagonal section. Similarly, the impact of the

thermal annealing on the morphology of ZnO NWs is not significant for an annealing temperature of 700 °C. However, a notable impact starts appearing from an annealing temperature of 800 °C, for which the pencil shape is kept but the hexagonal section is much less faceted. As the annealing temperature was further raised to 900 °C, the pencil shape is kept but the hexagonal section is lost with no facets. A progressive coalescence process of ZnO NWs is even revealed along with a merging process of the surfaces of nearby ZnO NWs, as the annealing time was increased from 1 to 2h. The occurrence of a coalescence process of ZnO NWs from an annealing temperature of 900 °C when grown by PLI-MOCVD is in agreement with the same process observed on ZnO NWs when grown by CBD.[33]

### 3.2. Effect of the post-deposition treatments on the electrical properties of ZnO nanowires

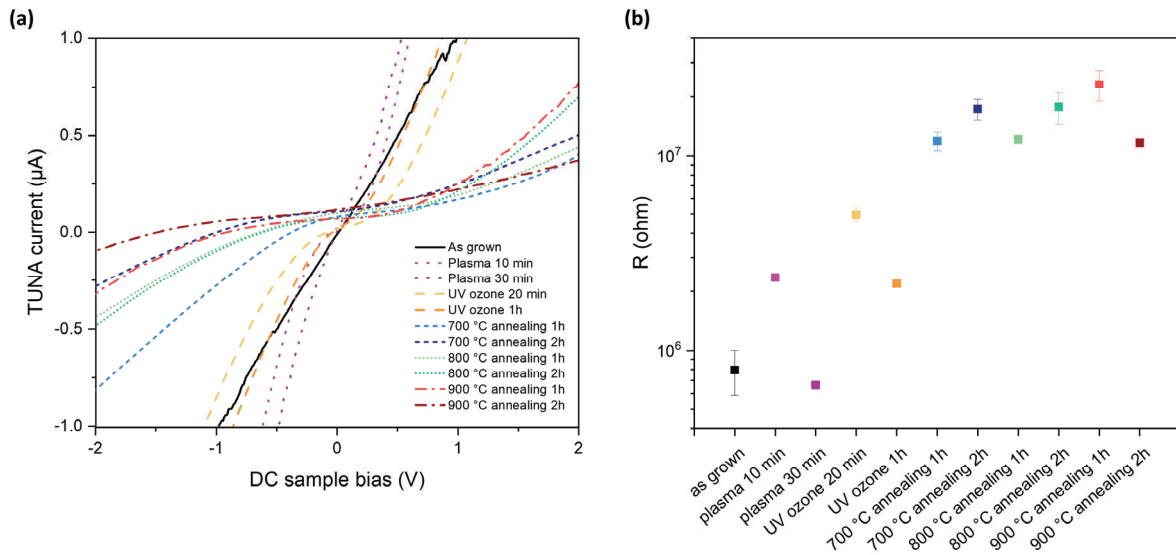


Figure 2. (a) TUNA current ( $I$ ) as a function of DC sample bias ( $V$ ) for ZnO NWs grown by PLI-MOCVD at 700 °C for 30 min, before and after post-deposition treatments. (b) Resistance estimated from the  $I$ - $V$  curve slope around 0 V as a function of post-deposition treatments.

The electrical properties of as-grown, treated, and thermally annealed ZnO NWs were assessed by TUNA measurements, as presented in Figure 2. Additional  $I$ - $V$  measurements are shown in Figure S7 of Supporting Materials. The  $I$ - $V$  curves shown in Figure 2a display the different electrical behaviors of ZnO NWs before and after each post-deposition treatment. The variation of the slope of the  $I$ - $V$  curve after post-deposition treatments is noticeable; however, to elaborate a more accurate comparison, an estimation of the resistance  $R$  of ZnO NWs was determined from the  $I$ - $V$  curve slope in the vicinity of 0 V. In this study, we assume that both contact resistances are negligible. The values are shown in Figure 2b, presenting the resistance  $R$  for the different post-deposition treatments. In Figure 2a, the first noticeable change in the electrical behavior of ZnO NWs is observed after thermal annealing, with a significant decrease in the slope around 0 V suggesting a decrease in their electrical

conductivity. This is validated in *Figure 2b* where the resistance  $R$  shows a significant increase, from approximately  $8 \times 10^5 \Omega$  to values around  $1 \times 10^7 \Omega$ . In contrast, the impact of the  $O_2$  plasma or UV ozone treatments is less significant. A transition from ohmic to Schottky-like behavior occurs after the  $O_2$  plasma treatment for 10 min, suggesting a decrease in the electrical conductivity of ZnO NWs. This is confirmed by the calculation of the resistance  $R$ , increasing from approximately  $8 \times 10^5$  to  $2 \times 10^6 \Omega$  after  $O_2$  plasma treatment. This is due to the adsorption of oxygen radicals from the plasma at the surface of the NW. However, following an  $O_2$  plasma treatment for 30 min, the ohmic behavior of ZnO NWs is retrieved with a slight increase in the slope and hence in their electrical conductivity, the resistance  $R$  reaching a value of approximately  $7 \times 10^5 \Omega$ . After UV ozone treatment, a transition from ohmic to Schottky-like behavior of ZnO NWs is also observed, leading to a decrease in their electrical conductivity, and therefore an increase in their resistance  $R$  from approximately  $8 \times 10^5 \Omega$  to values significantly above  $10^6 \Omega$ . This decrease is due to oxygen adsorption at the surfaces of the ZnO NWs, removing free electrons from the bulk. For both the  $O_2$  plasma and UV ozone treatments, the kinetics of the different physicochemical phenomena involved play a significant role on the electrical properties of ZnO NWs.

To complement this analysis, the density of free charge carriers  $n$  (electrons in this case) was estimated from the resistance  $R$  as follows:

$$n = \frac{1}{q\mu R A} \quad (1)$$

where  $l$  is the distance between the electrodes, in this case corresponding to the length of ZnO NWs of approximately  $2.5 \mu\text{m}$ ,  $A$  is the transverse section area of electrical conduction, as  $A = \pi r^2$  by assuming an electrical conduction through the entire radius of ZnO NWs,  $q$  is the electron charge and  $\mu$  is the mobility of free electrons. The range of values expected for the density of free electrons in as-grown ZnO NWs grown by PLI-MOCVD at  $700 \text{ }^\circ\text{C}$  is  $1.8 - 3.3 \times 10^{18} \text{ cm}^{-3}$  from 4-point probe resistivity measurements [25]. Therefore, the mobility of free electrons was roughly estimated in the range of  $3 - 10 \text{ cm}^2 \text{ V}^{-1} \text{ s}^{-1}$  from TUNA measurements. After thermal annealing, the density of free electrons of ZnO NWs decreases to values in the range of  $4 \times 10^{16} - 3 \times 10^{17} \text{ cm}^{-3}$ . After  $O_2$  plasma treatment for 10 minutes, the density of free electrons decreases to approximately  $4 \times 10^{17} - 1 \times 10^{18} \text{ cm}^{-3}$ . However, due to a decrease in the resistance  $R$  after a 30 minutes exposure and by supposing that the mobility of free electrons stays constant, the density of free electrons supposedly increases up to values in the same range as the as-grown ZnO NWs. This could suggest an increase in the free electron mobility value and no further decrease in the density of free electrons between 10 and 30

minutes of exposure. In the case of UV ozone treatment for 20 minutes, the density of free electrons decreases to values in the range of  $2 - 7 \times 10^{17} \text{ cm}^{-3}$ . A similar behavior as the one observed after plasma treatment is detected after increasing the duration of the treatment to 1 h, meaning once again an increase in the free electron mobility.

### 3.3. Effect of the post-deposition treatments on the optical properties of ZnO nanowires

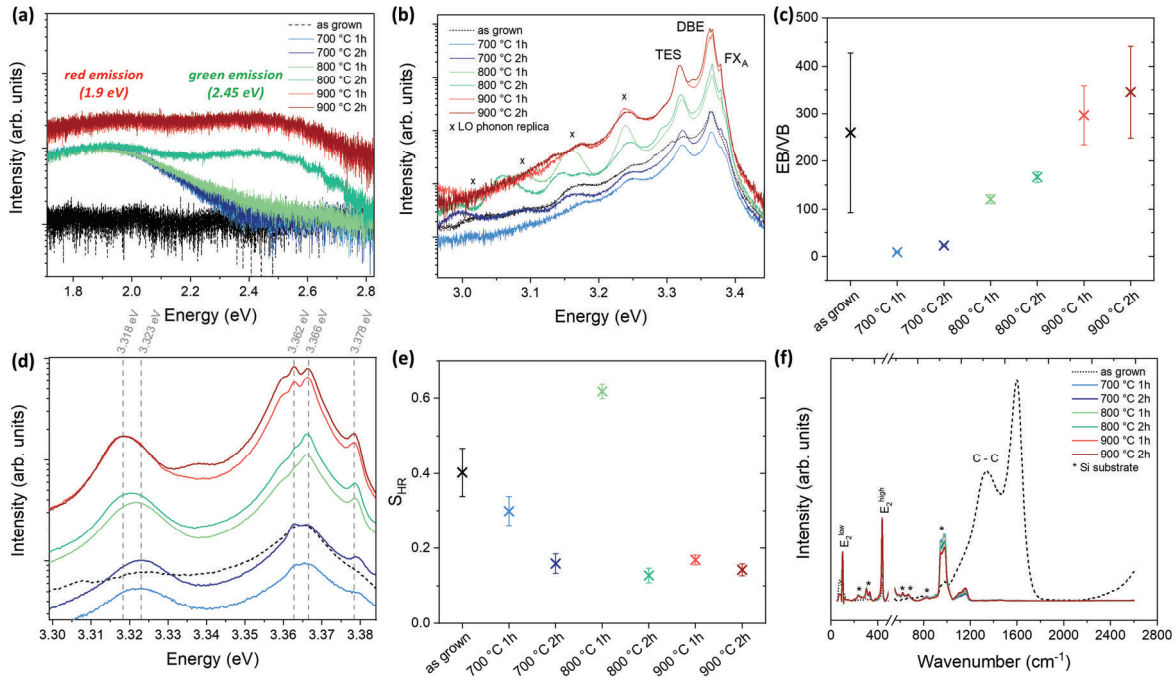


**Figure 3.** 5K CL spectra in continuous mode of ZnO NWs grown by PLI-MOCVD at 700 °C for 30 min, before and after thermal annealing, and plotted with a logarithmic intensity axis showing (a) the visible emission band between 1.6 and 2.8 eV and (b) the NBE between 3.0 and 3.5 eV. (c) Intensity ratio of the excitonic emission band over the visible emission band. (d) Zoom-in on the CL spectra between 3.30 and 3.38 eV (e) Huang-Rhys constant  $S_{HR}$  and (f) Raman spectra from 50 to 2600  $\text{cm}^{-1}$  for the as-grown ZnO NWs and after thermal annealing at 700 °C, 800 °C and 900 °C for 1 and 2h under  $\text{O}_2$  atmosphere.

The impact of the post-deposition treatments on the optical properties of ZnO NWs, and therefore on the nature and amount of their defects, is assessed by CL combined with Raman spectroscopy. Thermal annealing treatments exhibit noticeable alterations in the CL spectra, impacting both their shape and intensity. *Figure 3a* illustrates the visible emission band ranging from 1.6 to 2.8 eV. In contrast to the as-grown ZnO NWs, where the contribution of the visible emission band was negligible, the thermal annealing at 700 °C for 1 h led to a distinct increase in its contribution, featuring a non-structured emission band centered at 1.9 eV. This corresponds to a red-orange emission band, possibly due to oxygen interstitials ( $\text{O}_i$ ) originating from an excess of oxygen atoms coming from the  $\text{O}_2$  atmosphere used to perform the thermal annealing [34]. A further change was observed when the annealing temperature and duration were increased above 800 °C for 2 h, resulting in an additional contribution centered at 2.45 eV, associated with the green emission band

and suggesting strong phonon coupling [35]. This unstructured behavior of the green emission band potentially implies the introduction of point defects such as zinc or oxygen vacancies [36], [37], [38], [39], [40], [41], since the role of hydrogen-related defects [42] has been excluded in ZnO NWs grown by PLI-MOCVD [20]. In *Figure 3b*, the CL spectra depict the consistent shape of the near-band-edge emission (NBE), ranging from 3.0 to 3.5 eV, following thermal annealing. However, the intensity varies with both the annealing temperature and duration. The intensity ratio of the excitonic emission band over the visible emission band is shown in *Figure 3c*. This value can directly quantify the structural and optical quality of the ZnO NWs, showing a sharp decrease after thermal annealing at 700 °C, from 227 to 8 and 21, respectively for a 1 and 2 h thermal annealing. This could be explained by the introduction of point defects such as oxygen interstitials, as discussed previously, degrading the structural and optical quality of the ZnO NWs. Increasing the annealing temperature to 800 °C slightly improves this intensity ratio, to 111 for a 1 h thermal annealing and 163 for a 2 h thermal annealing, in the same range as the original value for as-grown ZnO NWs. However, a significant improvement proceeds when reaching an annealing temperature of 900 °C, almost doubling the intensity ratio to 336 after 1 h and 372 after 2 h. This effect is due to the surface modification of the hexagonal facets observed in the SEM images in *Figure 1*, likely reducing the concentration of non-radiative recombination centers and hence increasing the density of free and bound excitons. *Figure 3d* presents a zoom-in of the main contribution of the NBE, related to the radiative transitions of donor-bound excitons (DBEs), located around 3.364 eV for the as-grown ZnO NWs. The broadening of the NBE band as the annealing temperature is increased reveals that the contribution at 3.366 eV strengthens while an additional contribution occurs at around 3.362 eV. The first specific transition at 3.366 eV is assigned to the formation of surface excitons [43], [44], which is supported by Ref. [25] where its strengthening occurs as the mean diameter of ZnO NWs grown by PLI-MOCVD is decreased. Here, the increase in the intensity of surface excitons with the annealing temperature indicates a strong reduction of nonradiative recombination centers. The second specific transition at 3.362 eV could be attributed to the  $I_6$  line related to the incorporation of Al substituting for Zn sites as  $Al_{Zn}$  originating from the residual contamination in the chamber [45]. The presence of  $Z_3$  and  $Z_4$  lines linked to the incorporation of carbon species [46] is ruled out by the Raman spectrum in *Figure 3f*, which demonstrates the removal of carbon contamination through thermal annealing with no apparent dependence on the annealing temperature and duration. The free exciton contribution located around 3.378 eV and corresponding to the longitudinal free A-exciton states [45] also occurs in *Figure 3d*. The increase in its intensity as the annealing temperature is increased again shows the high structural and optical quality of ZnO NWs after thermal annealing, especially at 900 °C. Additionally, an increase of both  $E_2^{low}$  and  $E_2^{high}$  line intensity, respectively at 99 and 438  $cm^{-1}$

<sup>1</sup>, from as-grown to thermally-treated ZnO NWs was observed from the Raman spectra shown in *Figure 3f*, supporting the improvement of the crystallinity after thermal annealing. Furthermore, the modification of the stoichiometry of ZnO was assessed due to an increase by a factor of 2 of the  $E_2^{high} / E_2^{low}$  line ratio, without any significant dependence on the annealing temperature or duration. This increase suggests the introduction of point defects inside the structure, which could confirm the hypothesis of the introduction of zinc or oxygen vacancies due to the observation of the unstructured green band in the CL spectrum.

The next major contribution in the CL spectra of as-grown ZnO NWs is located at 3.323 eV, involving two-electron satellites (TES). However, *Figure 3d* shows that the shift of the TES line to lower energies as the annealing temperature is increased is due to an additional contribution at 3.318 eV, likely demonstrating the formation of basal-plane stacking faults (BSFs). The CL spectra in *Figure 3b* reveal distinctive peaks positioned at energy levels of approximately 3.251, 3.179, 3.107, and 3.035 eV, which correspond to the longitudinal optical (LO) phonon replicas of the TES line. These peaks exhibit a consistent energy separation of 72 meV related to the phonon energy in ZnO. The intensity of the LO phonon replicas follows a Poisson distribution, characterized by the following equation:

$$I_n = \frac{e^{-S} \cdot S^n}{n!} I_0 \quad (2)$$

where  $n$  represents the number of phonon replicas,  $I_n$  is the intensity of the  $n^{\text{th}}$  replica,  $I_0$  is the intensity of the TES line, and  $S_{HR}$  is the Huang-Rhys constant. This constant serves as a crucial parameter that reflects the strength of the coupling between the electronic transitions and LO polarization field. The determined values of  $S_{HR}$  for the different as-grown and thermally annealed ZnO NWs are shown in *Figure 3e*, showing a linear decrease from 0.4 to approximately 0.1 from the as-grown ZnO NWs to the thermally treated ZnO NWs at 700 °C for 2h. After increasing the annealing temperature, this value stays around 0.1, except for the one annealed for 1h at 800 °C, rising up to 0.6.

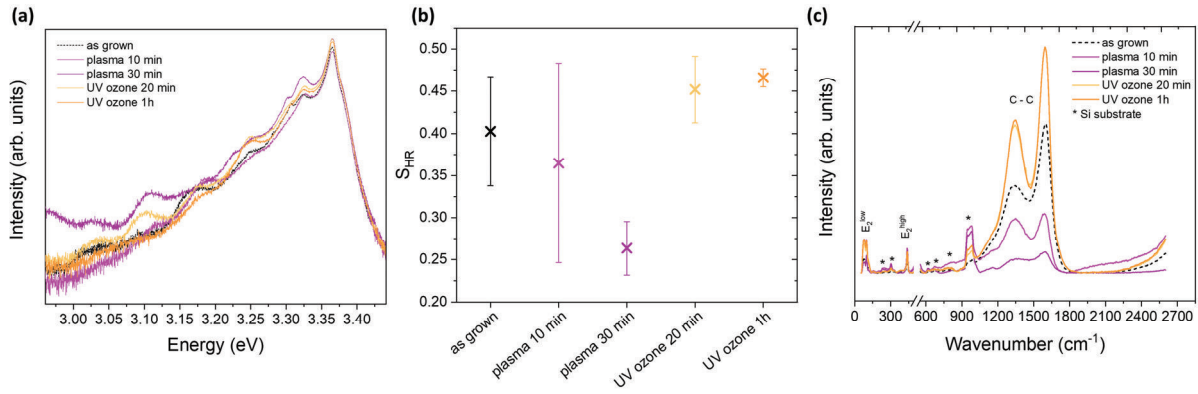
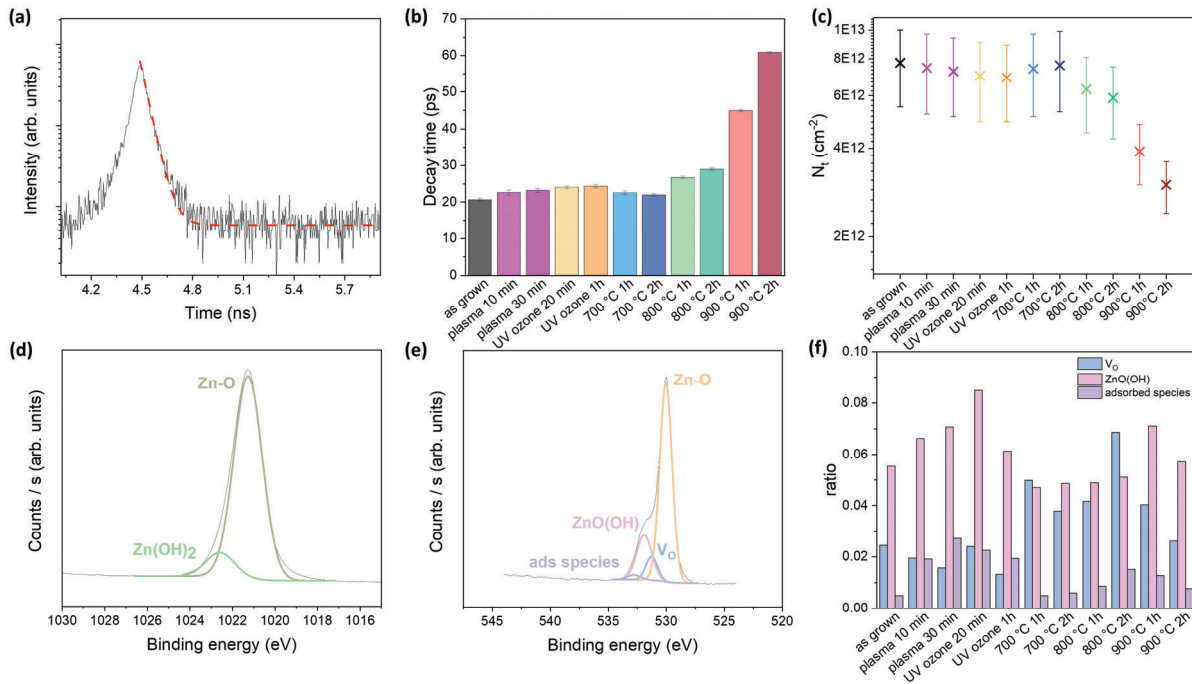


Figure 4. (a) 5K CL spectra in continuous mode of ZnO NWs grown by PLI-MOCVD at 700 °C for 30 min, before and after post-deposition treatments, and plotted with a logarithmic intensity axis showing the NBE between 3.0 and 3.5 eV. (b) Huang-Rhys constant  $S_{HR}$  and (c) Raman spectra from 50 to 2600  $cm^{-1}$  for the as-grown ZnO NWs and after plasma and UV ozone treatments for several exposure durations

The results depicted in Figure 4a show that, contrary to thermal annealing, both O<sub>2</sub> plasma and UV ozone treatments have a smaller impact on the shape and intensity of the CL spectra. The Huang-Rhys constant  $S_{HR}$  however varies with the type of post-deposition treatments and its exposure duration. As revealed in Figure 4b, the determined value of  $S_{HR}$  slightly decreases to 0.36 when the ZnO NWs are subjected to an O<sub>2</sub> plasma for 10 minutes, and more importantly decreases to 0.26 when increasing the exposure duration to 30 minutes. In contrast, the determined value of  $S_{HR}$  increases on average from 0.40 to 0.46 after UV ozone treatment of the ZnO NWs, with a smaller impact from the exposition duration. The same behavior is observed in Figure 4c reporting the Raman spectra of the as-grown and treated ZnO NWs. The intensity of the C-C peaks incrementally decreases as the exposure duration to O<sub>2</sub> plasma is increased, due to the oxygen radicals from the plasma reacting with and removing carbon species in the ZnO NWs. In contrast, an increase in the intensity of the C-C peaks occurs after UV ozone treatments. This phenomenon could arise from the creation of C-C bonds originating from carbon species present on the surface or within the bulk of the ZnO NWs, through some interactions with oxygen or hydrogen species. The correlation between these two results could assert the carbon contribution to the transitions associated with the TES line.



**Figure 5.** (a) Plot of the CL intensity decrease for ZnO NWs grown by PLI-MOCVD for 30 minutes and annealed at 900 °C for 1h, with the red dashed line showing a decreasing exponential fit. (b) Resulting decay time of ZnO NWs before and after post-deposition treatments. (c) Density of surface traps  $N_t$  in ZnO NWs before and after post-deposition treatments. XPS spectra of ZnO NWs grown by PLI-MOCVD for 30 minutes corresponding to the (d) Zn2p and (e) O1s core levels along with their respective fitting. (f) Fitted curve area ratio of O1s contributions over Zn-O contributions.

The surface properties before and after post-deposition treatments are assessed by time-resolved CL spectroscopy and supported with XPS measurements. An example of the resulting exponential decay of the CL intensity during these measurements is presented in *Figure 5a* in the case of ZnO NWs grown by PLI-MOCVD for 30 minutes and thermally annealed at 900 °C for 1h. The fitting of this curve with an exponential law as revealed with the red dashed line allowed us to deduce the associated decay time. Additional examples of the exponential decay of the CL intensity are presented in *Figure S8* of Supporting Materials. The value of the decay time of the CL intensity during time-resolved measurements, as a function of the different post-deposition treatments and their duration, is shown in *Figure 5b*. After plasma exposure for either 10 or 30 minutes, the decay time increases slightly from 20.5 ps to approximately 22.5 ps. After treating the ZnO NWs with UV ozone, this value increases to 24 ps. Following a 700 °C thermal annealing, this value also slightly increases to around 22 ps. However, with an increase of the annealing temperature to 800 °C, the decay time increases to 26.5 ps for a 1h annealing and to 29 ps for 2h. Elevating the annealing temperature further to 900 °C leads to a more substantial increase, resulting in decay time values of about 45 and 60 ps, for a 1 and 2h annealing time, respectively. This variation could be related to the fact that, while increasing the annealing temperature and time, the surface recombination becomes less and less significant. Indeed, the correlation between the effective lifetime  $\tau^*$  and the surface

recombination velocity  $S$  is described by the following equation, and demonstrates that an increase in the effective lifetime induces a decrease in the surface recombination velocity.

$$\frac{1}{\tau^*} = \frac{1}{\tau_B} + \frac{2S}{r - d_{spc}} \quad (3)$$

In this equation,  $\tau_B$  represents the exciton bulk lifetime, a constant value set at 10 ns for ZnO [47],  $r$  is the radius of the NW, here evaluated at 70 nm, and  $d_{spc}$  is the width of the charge carrier depletion region near the surface, which emerges as a consequence of the Fermi level pinning effect occurring at the NW surface. This last unknown was estimated with the help of COMSOL simulations, as explained in the Supplementary Information of [25]. The surface recombination velocity  $S$  is linked to the density of surface traps of the NWs, denoted  $N_t$ . This relationship is expressed as  $S = \sigma v_{th} N_t$ , where  $\sigma$  represents the capture cross-section of the recombination center, and  $v_{th}$  the thermal hole velocity. *Figure 5c* shows the value of  $N_t$  determined, as a function of the post-deposition treatment. In accordance with its inverse proportionality with the decay time, this value shows a small decrease from 7.7 to 7.3 x 10<sup>12</sup> cm<sup>-2</sup> after O<sub>2</sub> plasma treatment, and another small decrease to 7.0 x 10<sup>12</sup> cm<sup>-2</sup> after UV ozone treatment. After thermal annealing at 700 °C,  $N_t$  also shows a decrease to 7.5 x 10<sup>12</sup> cm<sup>-2</sup> compared to as grown NWs. Raising the annealing temperature to 800 °C decreases the value to 6.3 and 5.9 x 10<sup>12</sup> cm<sup>-2</sup>, respectively, for a 1h and 2h annealing time. At 900 °C, a more significant reduction occurs, reaching values of 3.9 x 10<sup>12</sup> cm<sup>-2</sup> after a 1h annealing and 3.0 x 10<sup>12</sup> cm<sup>-2</sup> after a 2h annealing.

The surface properties were further examined by XPS measurements. The results are shown in *Figure 5d-f*. In *Figure 5d*, the zinc related peaks corresponding to Zn-O and Zn(OH)<sub>2</sub> bonds for the as-grown ZnO NWs grown by PLI-MOCVD for 30 minutes are presented. In addition, *Figure 5e* shows the different contributions to the oxygen related core levels, corresponding to Zn-O, oxygen vacancies, ZnO(OH) and adsorbed species such as H<sub>2</sub>O, C-O or C=O, respectively located at 529.9 eV, 531.2 eV, 531.9 eV and 533 eV respectively [48]. In *Figure 5f*, the fitted curves area ratio of the different oxygen contributions with Zn-O are shown. After O<sub>2</sub> plasma treatment, the ratio of adsorbed species slightly increases with the exposure duration, suggesting the migration of carbon species from the bulk to the surfaces of ZnO NWs, as indicated in the Raman spectrum in *Figure 4c*. After UV ozone treatment, a similar behavior is observed, in this case due to the formation of new bonds between carbon, oxygen and hydrogen molecules at the surface of ZnO NWs. After thermal annealing, the ratio of oxygen vacancies follows a similar trend as the decay time for the 700 °C and 800 °C

annealing temperatures, validating to some extent the observed decrease in the density of surface traps. However, for 900 °C annealing, the proportion of oxygen vacancies does not increase further, but hydroxyl species ZnO(OH) ratio increases.

### 3.4. Effect of the post-deposition treatments on the piezoelectric properties of ZnO nanowires

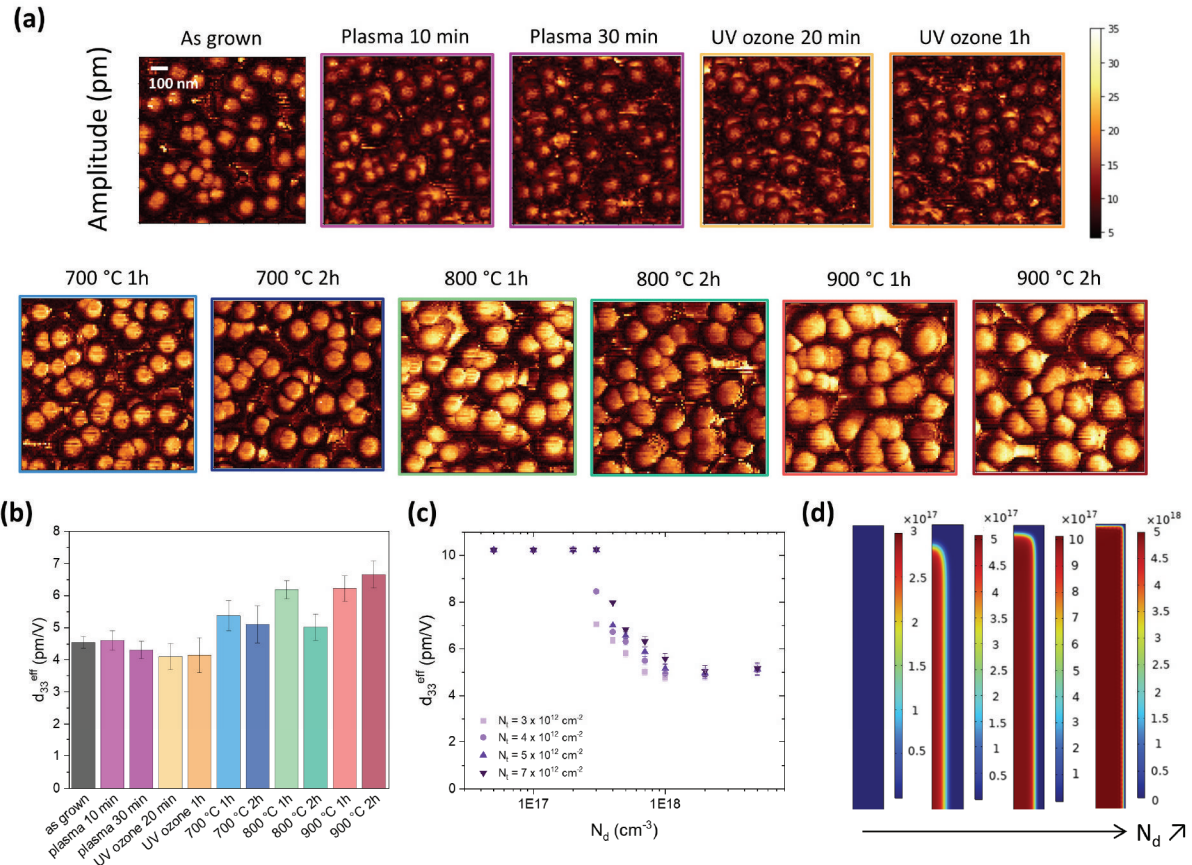


**Figure 6.** (a) PFM measurements displaying the amplitude of the piezoelectric response of ZnO NWs before and after post-deposition treatments. The scale bar denoted as 100 nm is valid for all the panels. (b)  $d_{33}^{eff}$  coefficient from PFM measurements of ZnO NWs before and after post-deposition treatments. (c) FEM simulations reporting the  $d_{33}^{eff}$  coefficient as a function of donor concentration  $N_d$  and of the density of surface traps  $N_t$ . (d) Electron concentration map focused on the top part of the ZnO NW (1  $\mu m$ ) for a given density of surface traps  $N_t = 5 \times 10^{12} cm^{-2}$  and as a function of the donor concentration  $N_d$  varying in the range of  $1 \times 10^{17}$  to  $5 \times 10^{18} cm^{-3}$ .

The amplitude of the piezoelectric response measured by PFM in the Datacube mode on the as-grown, treated, and thermally annealed ZnO NWs is shown in Figure 6a. The amplitude of the piezoelectric response is in the range of 0-35 pm, when a 5 V AC voltage is applied between the substrate and the conductive AFM tip.

In Figure 6b, the effective piezoelectric coefficient  $d_{33}^{eff}$  of ZnO NWs is plotted before and after post-deposition treatments. This coefficient is defined as the amplitude of the piezoelectric response divided by the applied AC voltage as follows:

$$d_{33}^{eff} = \frac{\text{Amplitude}}{\text{Applied Voltage}} \quad (4)$$

where the applied AC voltage is of 5 V. Prior to the determination of the mean value of  $d_{33}^{eff}$ , the piezoelectric amplitude was filtered as explained in the experimental procedure. The results from the as-grown ZnO NWs and those treated with plasma or UV ozone are in the same order of magnitude, showing low to no impact of these kind of treatments on their piezoelectric behavior. In contrast, the thermally annealed ZnO NWs show an incremental increase in their piezoelectric behavior as the annealing temperature was increased. Indeed, the 700 °C annealed ZnO NWs for 1h show a  $d_{33}^{eff}$  coefficient increase from approximately 4.5 to 5.4 pm/V on average. However, if annealed for 2h at the same temperature, this value drops to 5.1 pm/V. By increasing the annealing temperature of ZnO NWs to 800 °C, the  $d_{33}^{eff}$  coefficient value jumps to 6.2 pm/V, but decreases again to 5 pm/V when further increasing the annealing time to 2h. Finally, at an annealing temperature of 900 °C for ZnO NWs, this value increases up to 6.2 and 6.6 pm/V, respectively, for a 1 and 2h annealing time. Additional PFM measurements supporting the data are shown in Figure S9 of Supporting Materials.

The evolution of the  $d_{33}^{eff}$  coefficient of thermally annealed ZnO NWs does not comply with the decrease in the density of surface traps as the annealing temperature was increased, as predicted by FEM simulations where we expect a lower piezoelectric performance for a lower density of surface traps [16]. However, due to the screening effect, the density of free charge carriers here has a predominant impact on the piezoelectric response. As discussed before, the thermal annealing greatly affects the electrical conductivity of the ZnO NWs, reducing the density of free electrons  $n$ , and to that extent the donor concentration  $N_d$ . In order to account for the increase in the  $d_{33}^{eff}$  coefficient with the annealing temperature, FEM simulations were performed using COMSOL Multiphysics software. The model and equations used are presented in the Electronic Supporting Information [25]. The values of the density of surface traps  $N_t$  are fixed in the range of 3 to 7 x 10<sup>12</sup> cm<sup>-2</sup>, as determined from time-resolved CL measurements. The donor concentration  $N_d$  was varied from 5 x 10<sup>16</sup> to 5 x 10<sup>18</sup> cm<sup>-3</sup>. The mean piezoelectric response on top of the NW, just below the

simulated PFM tip, was calculated and used to determine the  $d_{33}^{eff}$  coefficient. The results are shown in *Figure 6c*. As expected, the  $d_{33}^{eff}$  coefficient decreases as  $N_d$  is increased, reaching a plateau from  $1 \times 10^{18} \text{ cm}^{-3}$ . However, the impact of the density of surface traps  $N_t$  is almost negated as  $N_d$  is increased above  $1 \times 10^{18} \text{ cm}^{-3}$  or decreased below  $2 \times 10^{17} \text{ cm}^{-3}$ . The effect of the donor concentration  $N_d$  also occurs in the electron concentration maps obtained from FEM simulation, as presented in *Figure 6d*. Only the top of the ZnO NW is presented to facilitate the visualization. We observe that, while  $N_t$  stays constant at the highest value of  $5 \times 10^{12} \text{ cm}^{-2}$ , the thickness of the depleted region significantly varies with  $N_d$ : on one side the ZnO NW is completely depleted for the smaller value, while on the other side an extremely thin depleted layer is formed for the higher value. This decrease in the depletion region thickness explains the reduction in the piezoelectric performance at high donor concentrations  $N_d$ . After thermal annealing at  $700 \text{ }^\circ\text{C}$ , the density of surface traps remains nearly unchanged, as reported in *Figure 5c*. Therefore, the increase of the  $d_{33}^{eff}$  value of ZnO NWs is essentially due to the decrease of the density of free electrons as shown using TUNA measurements. However, after thermal annealing at  $800$  and  $900 \text{ }^\circ\text{C}$ , an incremental decrease in the density of surface traps occurs on the one hand, which may induce a decrease in the piezoelectric response. TUNA measurements on the other hand showed a decrease in the density of free electrons for this annealing temperature range compared to as-grown ZnO NWs, remaining in the same order of magnitude as compared to the thermal annealing at  $700 \text{ }^\circ\text{C}$ . Therefore, the  $d_{33}^{eff}$  coefficient should decrease as the annealing temperature. However, we observe the opposite behavior, meaning that the impact of the density of surface traps in this range of values ( $3\text{--}7 \times 10^{12} \text{ cm}^{-2}$ ) is negligible. This increase could further result from the enhancement of the crystallinity of the ZnO NWs as supported by CL and Raman spectroscopy measurements, specifically following the  $900 \text{ }^\circ\text{C}$  thermal annealing. In addition, we assumed that the free electron mobility was constant in our calculation of the density of free electrons. Nevertheless, the free electron mobility may vary, and more specifically, we would expect an increase after thermal annealing [33]. According to the Equation 1, this increase in the free electron mobility would further support the hypothesis of a more significant decrease in the density of free electrons, likely explaining the increase in the piezoelectric performance of annealed ZnO NWs.

## 4. Discussion

A schematic diagram is presented in *Figure 7* to show the adjusted screening and surface effects related to the respective densities of free electrons and surface traps following the post-deposition treatments of ZnO NWs grown by PLI-MOCVD. Interestingly, the morphology of ZnO NWs is generally retained following the post-deposition treatments, except the thermal annealing from 800 °C where the hexagonal section is progressively less faceted and eventually lost with the further occurrence of a coalescence process from 900 °C. The present statement is in agreement with Refs. [33], [49] dedicated to the effects of the post-deposition treatments on the structural properties of ZnO NWs grown by CBD. Importantly, the as-grown ZnO NWs exhibit a density of free electrons in the range of  $1.8 - 3.3 \times 10^{18} \text{ cm}^{-3}$ , which is smaller than the effective critical concentration for the Mott transition [50] and hence shows a nonmetallic electrical conduction. The present range of values is in agreement with the expectations for ZnO NWs grown by MOCVD [51], [52], [53]. The nature of the predominantly formed point defects are assigned to  $\text{Al}_{\text{Zn}}$  and carbon species, through the presence of the  $I_6$  [45] and  $Z$  [46] lines using CL spectroscopy as well as to the C-C bonds using Raman spectroscopy. The involvement of carbon species in the *p*-type and *n*-type doping of ZnO has poorly been documented so far [54], [55], but their high concentration in most of the chemical deposition techniques could support their contribution to the electronic properties. Using density functional theory calculations, carbon substituting for Zn sites as  $\text{C}_{\text{Zn}}$  has for instance been reported as a donor with a relatively low formation energy [54], [56]. Also, surface excitons are expected to play a significant role in the NBE emission of as-grown ZnO NWs by PLI-MOCVD, through an emission line around 3.366 eV [44]. The surface trap density in as-grown ZnO NWs grown by PLI-MOCVD is around  $7.7 \times 10^{12} \text{ cm}^{-2}$ , and hence higher than the surface trap density in ZnO NWs typically grown by MOCVD around  $2 \times 10^{12} \text{ cm}^{-2}$  [57]. This is due to the different injection system of chemical precursors in PLI-MOCVD, as well as the lower growth temperature used. The nature of surface traps is still under debate, although oxygen atoms adsorbed on the surface and acting as acceptors have previously been suggested [57].

The  $\text{O}_2$  plasma and UV ozone treatments does not have a significant impact on the densities of free electrons and surface traps, which are slightly decreased below  $10^{18} \text{ cm}^{-3}$  and around  $7.0 \times 10^{12} \text{ cm}^{-2}$ , respectively. The  $\text{O}_2$  plasma treatment is however able to drastically reduce the number of C-C bonds on the surfaces of ZnO NWs, where oxygen radicals efficiently react with carbon species. This is in contrast with the UV ozone treatment increasing the number of C-C bonds on the surfaces of ZnO NWs, which is certainly due to the partial decomposition of chemical residues originating from the DEZn precursor. The correlated small effect on the density of surface traps indicate that the

predominant surface traps may not be related to carbon species. All in all, the  $d_{33}^{eff}$  coefficient of as-grown ZnO NWs and post-treated ZnO NWs with the O<sub>2</sub> plasma and UV ozone retains a fairly constant value in the range of 4 – 5 pm/V. More importantly, the thermal annealing under O<sub>2</sub> atmosphere exhibit a much more significant impact on the densities of free electrons and surface traps. As the annealing temperature is increased, the density of free electrons is found to decrease down to values in the range of  $4 \times 10^{16} - 3 \times 10^{17} \text{ cm}^{-3}$ . Following the removal of the C-C bonds on the surfaces of ZnO NWs, the predominantly formed point defect is assigned to Al<sub>Zn</sub> and no more to carbon species, through the presence of the I<sub>6</sub> line [45] using CL spectroscopy. Interestingly, the strengthening of surface excitons in the NBE emission of thermally annealed ZnO NWs further reveals the reduction of nonradiative recombination centers on their surfaces [44]. This is very well correlated with the drastic decrease in the density of surface traps down to values around  $3.0 \times 10^{12} \text{ cm}^{-2}$ . The concomitant increase in the concentration of V<sub>O</sub> as indicated by XPS again points the major role of oxygen atoms adsorbed on the surface and acting as acceptors on the predominantly formed surface traps [57]. Eventually, the  $d_{33}^{eff}$  coefficient of thermally annealed ZnO NWs undergoes a significant 47% increase up to values around 6.6 pm/V. This shows that the positive effect of the decrease in the density of free electrons dominates the negative effect of the decrease in the density of surface traps: in other words, the reduction of the screening of the piezoelectric potential by free electrons in the bulk of ZnO NWs is predominant over the increase in the passivation of the surface traps of ZnO NWs.



annealing, the voltage increased up to 8 V. Zhang et al. [65] deposited ZnO thin films on stainless steel using magnetron sputtering and deposited PMMA on top of the film to fabricate the piezoelectric devices. The devices consisted in suspended cantilevers that produced a voltage under vibration at their resonance frequency. The thermal annealing at different temperatures were applied on the ZnO thin films. Interestingly, the piezoelectric response of the devices was not systematically improved as the temperature was increased, for instance the un-treated devices produced ~125 mV in open circuit conditions. After thermal annealing at 150°C, the voltage increased to ~250 mV, but after thermal annealing at 250°C, the voltage generated dropped to ~50 mV. Pham et al. [63] reported the effect of thermal annealing on the piezoelectric performance of devices integrating vertical ZnO NWs grown by CBD on sapphire substrates. The devices were tested under vertical compression generating a voltage. After thermal annealing, the generated voltage increased from ~48 mV to ~300 mV. Villafuerte et al. [64] used CBD to grow ZnO NWs on PDMS substrates, and encapsulated them with PMMA to complete flexible piezoelectric devices. The piezoelectric coefficient of the devices was measured using a charge meter under mechanical solicitation. They found that the piezoelectric coefficient increased from 0.288 pC/N to 0.338 pC/N after thermal annealing. The details of these results are summarized in Table 1.

Growth method	Dimensions (L/D/Aspect ratio)	Characterization method	Sample	Post-treatment	Piezoelectric Performance	REF
CBD	250-300nm wide NWs.	AFM/current amplifier	Single NWs	As-grown	78 mV	[61]
				O <sub>2</sub> Plasma, 250W	122.7mV	
CBD	2μm/150nm/13.3	Bending, 012% strain @ 3.56%/s	Device integrating NWs	As-grown	2.5V	[62]
				O <sub>2</sub> Plasma, 30min@30W	5V	
				Annealing, Ambient condition, 30min@350°C	8V	
Magnetron Sputtering	655nm thick film. Integration into	Vibration at resonance, 11m/s <sup>2</sup>	Device integrating thin film	As-deposited	~125mV	[65]
				Annealing, 2h@150°C	~250mV	

	cantilevers.					
CBD	~900nm/50-200nm/4.5-18	Compression, 0.9kgf	Device integrating NWs	As-grown	~48mV	[63]
				Annealing, Air atmosphere, 30min@350°C	~300mV	
CBD	~1μm/70nm/14	Charge measurement under compression ( $d_{33}$ )	Device integrating NWs	As-grown	0.288pC/N	[64]
				Annealing, O <sub>2</sub> atmosphere, 2h@220°C	0.338pC/N	
MOCVD	2.5μm/140nm/17.8	PFM ( $d_{33}$ )	Single NWs	As-grown	4.5pm/V	This work
				Annealing, O <sub>2</sub> atmosphere (1h@900°C)	6.2pm/V	

**Table 1.** Performance of piezoelectric devices made of as-grown and post-deposition treated ZnO NWs.

Therefore, the present findings reveal that a trade-off between the decreased density of surface traps and the decreased density of free electrons should be found using the most appropriate post-deposition treatments. This suggests that the more sophisticated combination of several different post-deposition treatments may be an innovative approach to further enhance the piezoelectric performance of ZnO NWs.

## 5. Conclusion

The effects of the post-deposition treatments on the properties of ZnO NWs grown by PLI-MOCVD have been demonstrated for several techniques including O<sub>2</sub> plasma, UV ozone, and thermal annealing under O<sub>2</sub> atmosphere. The impact of such treatments on the density of free charge carriers has been determined by TUNA measurements, showing a sharp decrease after thermal annealing, from approximately  $1.8 - 3.3 \times 10^{18} \text{ cm}^{-3}$  down to values around  $10^{17} \text{ cm}^{-3}$  regardless of the temperature, as compared to O<sub>2</sub> plasma or UV ozone where only a small decrease has been observed. 5K CL measurements have shown the crystallinity improvement after thermal annealing, especially at 900 °C. The introduction of defects such as zinc or oxygen vacancies after thermal annealing has also been revealed. In contrast, the O<sub>2</sub> plasma and UV ozone treatments have shown a

lower impact on the CL spectra. The Raman scattering spectra have further revealed the thermal annealing as the most reliable way to remove the carbon contamination. Time-resolved CL measurements have shown a significant increase in the decay time of CL intensity after thermal annealing, especially at 900 °C. The density of surface traps has then been estimated, in the range of  $3.0 - 7.7 \times 10^{12} \text{ cm}^{-2}$ , showing a significant decrease as the annealing temperature was increased. Finally, the piezoelectric response of these ZnO NWs has been assessed by PFM measurements, showing the increase of the  $d_{33}^{eff}$  coefficient with the increase of the annealing temperature, up to a significant 47 % increase (from 4.5 to 6.6 pm/V) for a 900 °C annealing. This increase has been analyzed on the basis of FEM simulations, showing the dependence of the piezoelectric response on the density of free charge carriers as well as on the density of surface traps, and further allowing a better understanding on the influence of the ZnO NW crystallinity. An 800 °C annealing temperature represents an optimal trade-off for enhancing the piezoelectric performance, preventing the coalescence of ZnO NWs as observed after thermal annealing at 900 °C, while maintaining a faceted hexagonal structure. This study opens the way for the development of ZnO NW-based mechanical energy transducers with a strongly enhanced performance.

## Conflict of interest

There are no conflicts to declare.

## Data availability

The data supporting this article have been included as part of the ESI.

## Acknowledgments

This work was supported by the French National Research Agency through the project SCENIC (ANR-20-CE009-0005). L.L. held a doctoral fellowship from the project SCENIC. The authors further acknowledge the support by the French RENATECH network through the PTA technological platforms in Grenoble. This research has also benefited from some of the characterization equipment of the Grenoble INP-CMTC platform and from the facilities and expertise of the OPE)N(RA characterization platform of FMNT (FR 2542, fmnt.fr) supported by CNRS, Grenoble INP and UGA.

## References

- [1] M. Willander *et al.*, 'Zinc oxide nanorod based photonic devices: recent progress in growth, light emitting diodes and lasers', *Nanotechnology*, vol. 20, no. 33, p. 332001, Jul. 2009, doi: 10.1088/0957-4484/20/33/332001.

- [2] Y.-S. Choi, J.-W. Kang, D.-K. Hwang, and S.-J. Park, 'Recent Advances in ZnO-Based Light-Emitting Diodes', *IEEE Trans. Electron Devices*, vol. 57, no. 1, pp. 26–41, Jan. 2010, doi: 10.1109/TED.2009.2033769.
- [3] W. Tian, H. Lu, and L. Li, 'Nanoscale ultraviolet photodetectors based on onedimensional metal oxide nanostructures', *Nano Res.*, vol. 8, no. 2, pp. 382–405, Feb. 2015, doi: 10.1007/s12274-014-0661-2.
- [4] W. Ouyang, J. Chen, Z. Shi, and X. Fang, 'Self-powered UV photodetectors based on ZnO nanomaterials', *Appl. Phys. Rev.*, vol. 8, no. 3, p. 031315, Sep. 2021, doi: 10.1063/5.0058482.
- [5] Z. L. Wang, 'Towards Self-Powered Nanosystems: From Nanogenerators to Nanopiezotronics', *Adv. Funct. Mater.*, vol. 18, no. 22, pp. 3553–3567, 2008, doi: 10.1002/adfm.200800541.
- [6] C. Pan, J. Zhai, and Z. L. Wang, 'Piezotronics and Piezo-phototronics of Third Generation Semiconductor Nanowires', *Chem. Rev.*, vol. 119, no. 15, pp. 9303–9359, Aug. 2019, doi: 10.1021/acs.chemrev.8b00599.
- [7] H. Wei *et al.*, 'An overview of lead-free piezoelectric materials and devices', *J. Mater. Chem. C*, vol. 6, no. 46, pp. 12446–12467, 2018, doi: 10.1039/C8TC04515A.
- [8] C. R. Bowen, H. A. Kim, P. M. Weaver, and S. Dunn, 'Piezoelectric and ferroelectric materials and structures for energy harvesting applications', *Energy Environ. Sci.*, vol. 7, no. 1, pp. 25–44, 2014, doi: 10.1039/C3EE42454E.
- [9] A. Yu, H. Li, H. Tang, T. Liu, P. Jiang, and Z. L. Wang, 'Vertically integrated nanogenerator based on ZnO nanowire arrays', *Phys. Status Solidi RRL – Rapid Res. Lett.*, vol. 5, no. 4, pp. 162–164, 2011, doi: 10.1002/pssr.201105120.
- [10] Z. Wang, X. Pan, Y. He, Y. Hu, H. Gu, and Y. Wang, 'Piezoelectric Nanowires in Energy Harvesting Applications', *Adv. Mater. Sci. Eng.*, vol. 2015, p. e165631, Jun. 2015, doi: 10.1155/2015/165631.
- [11] Z. L. Wang and J. Song, 'Piezoelectric Nanogenerators Based on Zinc Oxide Nanowire Arrays', *Science*, vol. 312, no. 5771, pp. 242–246, Apr. 2006, doi: 10.1126/science.1124005.
- [12] G. Zhu, R. Yang, S. Wang, and Z. L. Wang, 'Flexible High-Output Nanogenerator Based on Lateral ZnO Nanowire Array', *Nano Lett.*, vol. 10, no. 8, pp. 3151–3155, Aug. 2010, doi: 10.1021/nl101973h.
- [13] A. Janotti and C. G. V. de Walle, 'Fundamentals of zinc oxide as a semiconductor', *Rep. Prog. Phys.*, vol. 72, no. 12, p. 126501, Oct. 2009, doi: 10.1088/0034-4885/72/12/126501.
- [14] G. Romano, G. Mantini, A. D. Carlo, A. D'Amico, C. Falconi, and Z. L. Wang, 'Piezoelectric potential in vertically aligned nanowires for high output nanogenerators', *Nanotechnology*, vol. 22, no. 46, p. 465401, Oct. 2011, doi: 10.1088/0957-4484/22/46/465401.
- [15] A. J. L. Garcia, M. Mouis, A. Cresti, R. Tao, and G. Ardila, 'Influence of slow or fast surface traps on the amplitude and symmetry of the piezoelectric response of semiconducting-nanowire-based transducers', *J. Phys. Appl. Phys.*, vol. 55, no. 40, p. 405502, Aug. 2022, doi: 10.1088/1361-6463/ac8251.
- [16] A. J. Lopez Garcia, M. Mouis, V. Consonni, and G. Ardila, 'Dimensional Roadmap for Maximizing the Piezoelectrical Response of ZnO Nanowire-Based Transducers: Impact of Growth Method', *Nanomaterials*, vol. 11, no. 4, Art. no. 4, Apr. 2021, doi: 10.3390/nano11040941.
- [17] Y. Liu *et al.*, 'Ultraviolet detectors based on epitaxial ZnO films grown by MOCVD', *J. Electron. Mater.*, vol. 29, no. 1, pp. 69–74, Jan. 2000, doi: 10.1007/s11664-000-0097-1.
- [18] W. Lee, M.-C. Jeong, and J.-M. Myoung, 'Catalyst-free growth of ZnO nanowires by metal-organic chemical vapour deposition (MOCVD) and thermal evaporation', *Acta Mater.*, vol. 52, no. 13, pp. 3949–3957, Aug. 2004, doi: 10.1016/j.actamat.2004.05.010.
- [19] W. i. Park, G.-C. Yi, M. Kim, and S. j. Pennycook, 'ZnO Nanoneedles Grown Vertically on Si Substrates by Non-Catalytic Vapor-Phase Epitaxy', *Adv. Mater.*, vol. 14, no. 24, pp. 1841–1843, 2002, doi: 10.1002/adma.200290015.
- [20] Q. C. Bui *et al.*, 'Morphology Transition of ZnO from Thin Film to Nanowires on Silicon and its Correlated Enhanced Zinc Polarity Uniformity and Piezoelectric Responses', *ACS Appl. Mater. Interfaces*, vol. 12, no. 26, pp. 29583–29593, Jul. 2020, doi: 10.1021/acsami.0c04112.

- [21] G. Malandrino, M. Blandino, M. E. Fragala, M. Losurdo, and G. Bruno, 'Relationship between Nanostructure and Optical Properties of ZnO Thin Films', *J. Phys. Chem. C*, vol. 112, no. 26, pp. 9595–9599, Jul. 2008, doi: 10.1021/jp8001492.
- [22] C. Sartel *et al.*, 'Surface morphology and photoluminescence studies of Sb-doped ZnO layers grown using MOCVD', *Phys. Status Solidi B*, vol. 247, no. 7, pp. 1687–1690, 2010, doi: 10.1002/pssb.200983693.
- [23] J.-P. Sénateur, C. Dubourdieu, F. Weiss, M. Rosina, and A. Abrutis, 'Pulsed injection MOCVD of functional electronic oxides', *Adv. Mater. Opt. Electron.*, vol. 10, no. 3–5, pp. 155–161, 2000, doi: 10.1002/1099-0712(200005/10)10:3/5<155::AID-AMO406>3.0.CO;2-2.
- [24] Q. C. Bui *et al.*, 'Influence of the AZO Electrode on ZnO Nanowire Growth by PLI-MOCVD and Related Piezoelectric Performance: Implications for Mechanical Energy Transducers', *ACS Appl. Nano Mater.*, vol. 6, no. 9, pp. 7436–7445, May 2023, doi: 10.1021/acsnm.3c00608.
- [25] L. Legardinier *et al.*, 'Dimensionality Effect on Surface States and Piezoelectric Behavior in ZnO Nanowires Grown by Pulsed-Liquid Injection Metal–Organic Chemical Vapor Deposition', *ACS Appl. Electron. Mater.*, Aug. 2024, doi: 10.1021/acsaelm.4c00549.
- [26] K. Sugiyama, H. Ishii, Y. Ouchi, and K. Seki, 'Dependence of indium–tin–oxide work function on surface cleaning method as studied by ultraviolet and x-ray photoemission spectroscopies', *J. Appl. Phys.*, vol. 87, no. 1, pp. 295–298, Jan. 2000, doi: 10.1063/1.371859.
- [27] B. J. Coppa *et al.*, 'Structural, microstructural, and electrical properties of gold films and Schottky contacts on remote plasma-cleaned, n-type ZnO{0001} surfaces', *J. Appl. Phys.*, vol. 97, no. 10, p. 103517, May 2005, doi: 10.1063/1.1898436.
- [28] Q. C. Bui *et al.*, 'Effects of thermal annealing on the structural and electrical properties of ZnO thin films for boosting their piezoelectric response', *J. Alloys Compd.*, vol. 870, p. 159512, Jul. 2021, doi: 10.1016/j.jallcom.2021.159512.
- [29] W. Xu, J. Jiang, L. Han, and X. Feng, 'Highly efficient UV-Ozone treatment for IAZO active layer to facilitate the low temperature fabrication of high performance thin film transistors', *Ceram. Int.*, vol. 46, no. 11, Part A, pp. 17295–17299, Aug. 2020, doi: 10.1016/j.ceramint.2020.04.016.
- [30] A. J. L. Garcia *et al.*, 'Size and Semiconducting Effects on the Piezoelectric Performances of ZnO Nanowires Grown onto Gravure-Printed Seed Layers on Flexible Substrates', *Nanoenergy Adv.*, vol. 2, no. 2, Art. no. 2, Jun. 2022, doi: 10.3390/nanoenergyadv2020008.
- [31] L. Jaloustre *et al.*, 'Toward Quantitative Measurements of Piezoelectricity in III-N Semiconductor Nanowires', *ACS Appl. Nano Mater.*, vol. 4, no. 1, pp. 43–52, Jan. 2021, doi: 10.1021/acsnm.0c02078.
- [32] S. Kim, D. Seol, X. Lu, M. Alexe, and Y. Kim, 'Electrostatic-free piezoresponse force microscopy', *Sci. Rep.*, vol. 7, no. 1, Art. no. 1, Jan. 2017, doi: 10.1038/srep41657.
- [33] J. Villafuerte *et al.*, 'Engineering nitrogen- and hydrogen-related defects in ZnO nanowires using thermal annealing', *Phys. Rev. Mater.*, vol. 5, no. 5, p. 056001, May 2021, doi: 10.1103/PhysRevMaterials.5.056001.
- [34] C. H. Ahn, Y. Y. Kim, D. C. Kim, S. K. Mohanta, and H. K. Cho, 'A comparative analysis of deep level emission in ZnO layers deposited by various methods', *J. Appl. Phys.*, vol. 105, no. 1, p. 013502, Jan. 2009, doi: 10.1063/1.3054175.
- [35] R. Chen *et al.*, 'Investigation of Structured Green-Band Emission and Electron–Phonon Interactions in Vertically Aligned ZnO Nanowires', *J. Phys. Chem. C*, vol. 114, no. 41, pp. 17889–17893, Oct. 2010, doi: 10.1021/jp1064209.
- [36] K. Vanheusden, C. H. Seager, W. L. Warren, D. R. Tallant, and J. A. Voigt, 'Correlation between photoluminescence and oxygen vacancies in ZnO phosphors', *Appl. Phys. Lett.*, vol. 68, no. 3, pp. 403–405, Jan. 1996, doi: 10.1063/1.116699.
- [37] X. H. Huang, C. Zhang, C. B. Tay, T. Venkatesan, and S. J. Chua, 'Green luminescence from Cu-doped ZnO nanorods: Role of Zn vacancies and negative thermal quenching', *Appl. Phys. Lett.*, vol. 102, no. 11, p. 111106, Mar. 2013, doi: 10.1063/1.4798240.

- [38] F. Leiter, H. Zhou, F. Henecker, A. Hofstaetter, D. M. Hofmann, and B. K. Meyer, 'Magnetic resonance experiments on the green emission in undoped ZnO crystals', *Phys. B Condens. Matter*, vol. 308–310, pp. 908–911, Dec. 2001, doi: 10.1016/S0921-4526(01)00837-7.
- [39] K. Vanheusden, W. L. Warren, C. H. Seager, D. R. Tallant, J. A. Voigt, and B. E. Gnade, 'Mechanisms behind green photoluminescence in ZnO phosphor powders', *J. Appl. Phys.*, vol. 79, no. 10, pp. 7983–7990, May 1996, doi: 10.1063/1.362349.
- [40] Y. W. Heo, D. P. Norton, and S. J. Pearton, 'Origin of green luminescence in ZnO thin film grown by molecular-beam epitaxy', *J. Appl. Phys.*, vol. 98, no. 7, p. 073502, Oct. 2005, doi: 10.1063/1.2064308.
- [41] F. H. Leiter, H. R. Alves, A. Hofstaetter, D. M. Hofmann, and B. K. Meyer, 'The Oxygen Vacancy as the Origin of a Green Emission in Undoped ZnO', *Phys. Status Solidi B*, vol. 226, no. 1, pp. R4–R5, Jul. 2001, doi: 10.1002/1521-3951(200107)226:1<R4::AID-PSSB99994>3.0.CO;2-F.
- [42] J. Villafuerte *et al.*, 'Zinc Vacancy–Hydrogen Complexes as Major Defects in ZnO Nanowires Grown by Chemical Bath Deposition', *J. Phys. Chem. C*, vol. 124, no. 30, pp. 16652–16662, Jul. 2020, doi: 10.1021/acs.jpcc.0c04264.
- [43] S. Jabri *et al.*, 'Adsorbed Molecules and Surface Treatment Effect on Optical Properties of ZnO Nanowires Grown by MOCVD', *J. Electron. Mater.*, vol. 46, no. 7, pp. 4690–4694, Jul. 2017, doi: 10.1007/s11664-017-5459-z.
- [44] L. Wischmeier *et al.*, 'Dynamics of surface-excitonic emission in ZnO nanowires', *Phys. Rev. B*, vol. 74, no. 19, p. 195333, Nov. 2006, doi: 10.1103/PhysRevB.74.195333.
- [45] B. K. Meyer *et al.*, 'Bound exciton and donor–acceptor pair recombinations in ZnO', *Phys. Status Solidi B*, vol. 241, no. 2, pp. 231–260, 2004, doi: 10.1002/pssb.200301962.
- [46] F. Mohammadbeigi, E. S. Kumar, S. Alagha, I. Anderson, and S. P. Watkins, 'Carbon related donor bound exciton transitions in ZnO nanowires', *J. Appl. Phys.*, vol. 116, no. 5, p. 053516, Aug. 2014, doi: 10.1063/1.4892090.
- [47] M. Noltemeyer *et al.*, 'Excitonic transport in ZnO', *J. Mater. Res.*, vol. 27, no. 17, pp. 2225–2231, Sep. 2012, doi: 10.1557/jmr.2012.139.
- [48] I. Gromyko, M. Krunk, T. Dedova, A. Katerski, D. Klauson, and I. Oja Acik, 'Surface properties of sprayed and electrodeposited ZnO rod layers', *Appl. Surf. Sci.*, vol. 405, pp. 521–528, May 2017, doi: 10.1016/j.apsusc.2017.02.065.
- [49] A. Dieulesaint *et al.*, 'Tunable Hydrogen-Related Defects in ZnO Nanowires Using Oxygen Plasma Treatment by Ion Energy Adjustment', *Nanomaterials*, vol. 14, no. 14, Art. no. 14, Jan. 2024, doi: 10.3390/nano14141225.
- [50] S. Brochen *et al.*, 'Non-metal to metal transition in n-type ZnO single crystal materials', *J. Appl. Phys.*, vol. 121, no. 9, p. 095704, Mar. 2017, doi: 10.1063/1.4977506.
- [51] A. D. L. Bugallo, F. Donatini, C. Sartel, V. Sallet, and J. Pernot, 'Metallic core conduction in unintentionally doped ZnO nanowire', *Appl. Phys. Express*, vol. 8, no. 2, p. 025001, Jan. 2015, doi: 10.7567/APEX.8.025001.
- [52] L. Wang *et al.*, 'Access to residual carrier concentration in ZnO nanowires by calibrated scanning spreading resistance microscopy', *Appl. Phys. Lett.*, vol. 108, no. 13, p. 132103, Mar. 2016, doi: 10.1063/1.4945100.
- [53] M. den Hertog *et al.*, 'In situ biasing and off-axis electron holography of a ZnO nanowire', *Nanotechnology*, vol. 29, no. 2, p. 025710, Dec. 2017, doi: 10.1088/1361-6528/aa923c.
- [54] S. T. Tan, X. W. Sun, Z. G. Yu, P. Wu, G. Q. Lo, and D. L. Kwong, 'p-type conduction in unintentional carbon-doped ZnO thin films', *Appl. Phys. Lett.*, vol. 91, no. 7, p. 072101, Aug. 2007, doi: 10.1063/1.2768917.
- [55] K. Tang *et al.*, 'Suppression of compensation from nitrogen and carbon related defects for p-type N-doped ZnO', *Appl. Phys. Lett.*, vol. 95, no. 19, p. 192106, Nov. 2009, doi: 10.1063/1.3262965.
- [56] S. Sakong and P. Kratzer, 'Density functional study of carbon doping in ZnO', *Semicond. Sci. Technol.*, vol. 26, no. 1, p. 014038, Dec. 2010, doi: 10.1088/0268-1242/26/1/014038.

- [57] F. Donatini *et al.*, 'Comparison of Three E-Beam Techniques for Electric Field Imaging and Carrier Diffusion Length Measurement on the Same Nanowires', *Nano Lett.*, vol. 16, no. 5, pp. 2938–2944, May 2016, doi: 10.1021/acs.nanolett.5b04710.
- [58] V. N. Popok, M. Chirumamilla, T. Krekeler, M. Ritter, and K. Pedersen, 'Magnetron Sputter Grown AlN Nanostructures with Giant Piezoelectric Response toward Energy Generation', *ACS Appl. Nano Mater.*, vol. 6, no. 10, pp. 8849–8856, May 2023, doi: 10.1021/acsanm.3c01250.
- [59] T. K. Sodhi *et al.*, 'Surface Charge: An Advantage for the Piezoelectric Properties of GaN Nanowires', *Nanoenergy Adv.*, vol. 4, no. 2, Art. no. 2, Jun. 2024, doi: 10.3390/nanoenergyadv4020008.
- [60] T. Jalabert, M. Pusty, M. Mouis, and G. Ardila, 'Investigation of the diameter-dependent piezoelectric response of semiconducting ZnO nanowires by Piezoresponse Force Microscopy and FEM simulations', *Nanotechnology*, vol. 34, no. 11, p. 115402, Jan. 2023, doi: 10.1088/1361-6528/acac35.
- [61] M. Hussain, M. A. Abbasi, Z. H. Ibupoto, O. Nur, and M. Willander, 'The improved piezoelectric properties of ZnO nanorods with oxygen plasma treatment on the single layer graphene coated polymer substrate', *Phys. Status Solidi A*, vol. 211, no. 2, pp. 455–459, 2014, doi: 10.1002/pssa.201300330.
- [62] Y. Hu, L. Lin, Y. Zhang, and Z. L. Wang, 'Replacing a Battery by a Nanogenerator with 20 V Output', *Adv. Mater.*, vol. 24, no. 1, pp. 110–114, 2012, doi: 10.1002/adma.201103727.
- [63] T. Toan Pham *et al.*, 'Reliable operation of a nanogenerator under ultraviolet light via engineering piezoelectric potential', *Energy Environ. Sci.*, vol. 6, no. 3, pp. 841–846, 2013, doi: 10.1039/C2EE23980A.
- [64] J. Villafuerte *et al.*, 'Boosting the piezoelectric coefficients of flexible dynamic strain sensors made of chemically-deposited ZnO nanowires using compensatory Sb doping', *Nano Energy*, vol. 114, p. 108599, Sep. 2023, doi: 10.1016/j.nanoen.2023.108599.
- [65] X. Zhang *et al.*, 'Effect of post-annealing on microstructure and piezoelectric properties of ZnO thin film for triangular shaped vibration energy harvester', *Surf. Coat. Technol.*, vol. 361, pp. 123–129, Mar. 2019, doi: 10.1016/j.surfcoat.2019.01.036.
- [66] R. Hinchet, S. Lee, G. Ardila, L. Montès, M. Mouis, and Z. L. Wang, 'Performance Optimization of Vertical Nanowire-based Piezoelectric Nanogenerators', *Adv. Funct. Mater.*, vol. 24, no. 7, pp. 971–977, 2014, doi: 10.1002/adfm.201302157.